

Platelet Membrane Biomimetic Chemiluminescent Nanoparticles for Targeted Therapy of Atherosclerosis

Qianru Zhou,[#] Maoqing Huang,[#] Yujie Wang, and Dan Mu*Cite This: *ACS Appl. Mater. Interfaces* 2025, 17, 46680–46692

Read Online

ACCESS |



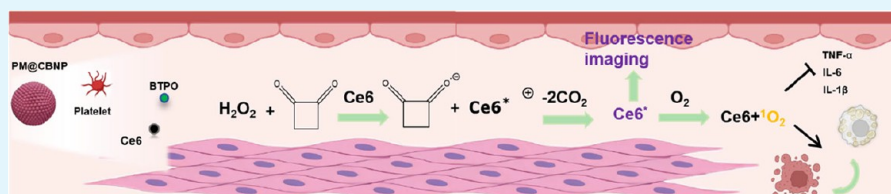
Metrics & More



Article Recommendations



Supporting Information



ABSTRACT: Photodynamic therapy (PDT) scavenges diseased cells by using photosensitizers, excitation light, and oxygen. Conventional PDT relies on external excitation light. The depth of penetration of the excitation light is limited, and atherosclerotic plaques are located deep in the tissue, which is not conducive to atherosclerosis treatment. In this study, self-luminescent nanoparticles, platelet membrane (PM)-coated PLGA nanoparticles containing the photosensitizer chlorin e6 (Ce6) and bis(2,4,5-trichloro-6-[pentyloxycarbonyl]phenyl)oxalate (BTPO) (PM@CBNP), are designed for atherosclerosis therapy. After PM@CBNP targeted the plaque, BTPO reacts with H₂O₂, exciting Ce6 to generate singlet oxygen (¹O₂) in the atherosclerotic plaque with overexpressed H₂O₂. The targeting ability and chemiluminescence of PM@CBNP are investigated in vitro and in vivo. In atherosclerotic mice, PM@CBNP eliminate inflammatory macrophages, reduce the expression of inflammatory factors, and prevent the progression of atherosclerosis. PM@CBNP provide an idea for the therapy of atherosclerosis.

KEYWORDS: atherosclerosis, photodynamic therapy, nanoparticles, chemical luminescence, targeted therapy

INTRODUCTION

Atherosclerosis (AS), the main pathologic basis of cardiovascular disease, has evolved over decades and still faces many challenges in its therapeutic strategies.^{1–3} Current clinical interventions include lipid-lowering statins, anti-inflammatory therapies, and interventional procedures, but these approaches have significant limitations in terms of targeting, long-term efficacy, and complication control.⁴ Recent studies have shown that the pathologic complexity of AS involves not only lipid metabolism disorders but is also closely related to chronic inflammation,^{5,6} oxidative stress, and plaque microenvironmental imbalances characterized by elevated hydrogen peroxide (H₂O₂) levels due to activated macrophages and oxidative stress.

The onset of AS is often closely related to other diseases, such as hypertension and hyperlipidemia. Under the influence of these factors, the vascular endothelium is damaged, expressing endothelial adhesion molecules (VCAM-1, ICAM-1), recruiting monocytes and T cells to infiltrate the intima. LDL in the blood penetrates the subendothelial layer and is oxidized by ROS to form ox-LDL. Macrophages phagocytose ox-LDL and transform into foam cells, forming early lipid streaks. Lipid overload promotes macrophage polarization toward the M1 type, leading to the secretion of proinflammatory factors (TNF- α , IL-6). Concurrently, the NF- κ B and NLRP3 inflammasome pathways are activated, promoting

IL-1 β release and maintaining the inflammatory microenvironment. Under inflammatory stimulation, enhanced metabolism in endothelial cells and macrophages leads to increased leakage of reactive oxygen species (ROS) from the mitochondrial electron transport chain (ETC). Superoxide anions (\cdot O₂[−]) are converted into H₂O₂ by superoxide dismutase (SOD). Lipid deposition, such as ox-LDL, disrupts mitochondrial β -oxidation, further increasing the level of ROS/H₂O₂ production. H₂O₂ can further oxidize LDL, damage the endothelium, and activate inflammation, forming a vicious cycle of “lipid-inflammation-oxidation.”

Song et al. achieved real-time monitoring of H₂O₂ concentration and polarity changes in plaques with the infrared ratio probe Cy7P-B.⁷ In the process, Song et al. found that H₂O₂ concentration was significantly elevated in the pathological microenvironment of AS, and the concentration of H₂O₂ within plaques could reach >50 μ M, which was 5–10 times higher than that of normal tissues. Although novel biologics have significantly improved low-density lipoprotein

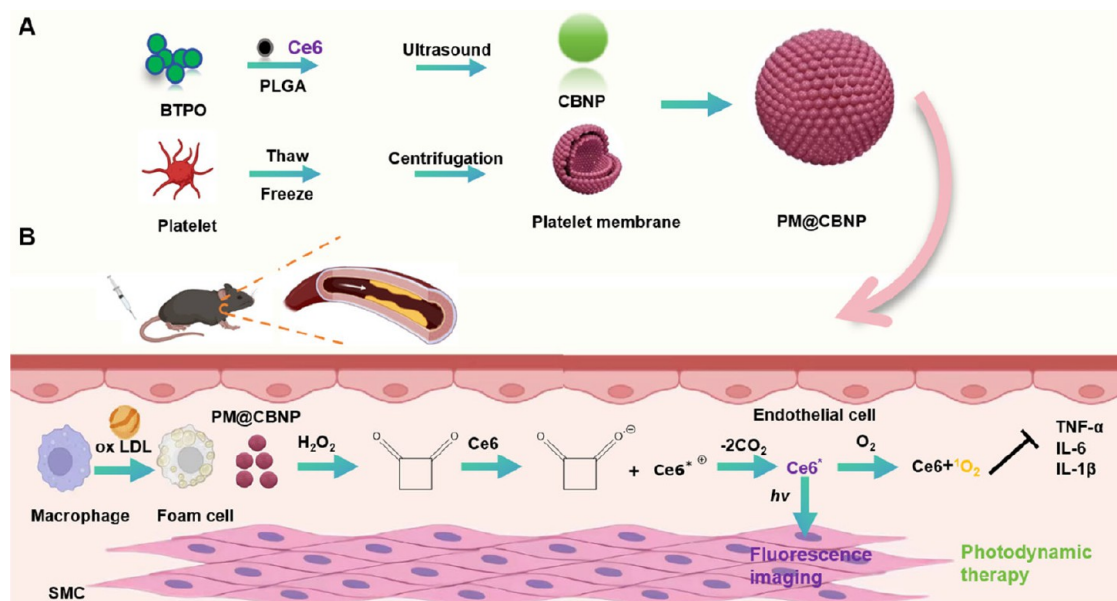
Received: May 22, 2025

Revised: August 1, 2025

Accepted: August 1, 2025

Published: August 11, 2025



Scheme 1. Preparation and Mechanism of PM@CBNP^a^a(A) Preparation and synthesis of PM@CBNP. (B) Principle of action in vivo of PDT.

(LDL) clearance efficiency, they are still unable to effectively address the core issues of macrophage foaming and inflammatory cascades within the plaque.⁸ Therefore, the development of therapeutic strategies that combine precise modulation and multifunctional synergy is urgent.

The unique physicochemical properties of nanomaterials provide novel ideas to break through the bottleneck of traditional therapies. For example, lipid-^{9,10} or polymer-based nanoparticles¹¹ can be surface-modified with targeting molecules to achieve specific enrichment of drugs at the plaque site.¹² In addition, responsive nanocarriers can precisely release anti-inflammatory drugs or apolipoproteins that promote reverse cholesterol transport, significantly enhancing plaque stability.^{13,14} More notably, multifunctional nanoplateforms can integrate the functions of imaging and therapy, such as nanoprobe that synergize near-infrared fluorescence imaging (NIRF),¹⁵ photoacoustic therapy (PAT),¹⁶ photothermal therapy (PTT),¹⁷ and photodynamic therapy (PDT), which provide real-time monitoring of plaque progression and precise interventions. Among them, PDT is a popular treatment that, unlike invasive treatments such as surgery, is safer and more specific.^{18,19} During PDT, photosensitizers can jump from the ground state to the excited state under light excitation. The excited photosensitizer at the lesion site undergoes a series of reactions to produce a large amount of singlet oxygen (¹O₂), which are cytotoxic and may cause cell autophagy. Traditional PDT is ill-suited for AS treatment primarily due to two critical limitations: (1) the deep-seated vascular location of atherosclerotic plaques, which are embedded 2–3 mm beneath the endothelium, and (2) the shallow tissue penetration depth of external excitation light (typically <1 cm), which hinders effective energy delivery to the lesion site. These constraints collectively result in inadequate targeting and suboptimal therapeutic efficacy for deep vascular lesions.²⁰

Many research teams have conducted very in-depth studies on both photodynamics and targeting. Hu et al. synthesized TPA-N.²¹ TPA is a lipophilic material, and photostability is

increased by combining it with N. TPA-N has been used as a fluorescent probe for the cellular level and has been shown to be superior to conventional fluorescent probes. It was demonstrated that at the cellular level, the fluorescence signal of TPA-N was superior to that of conventional lipid droplet fluorescent probes. Meanwhile, in in vivo experiments, TPA-N was highly enriched in adipose tissue. Similarly, TPE is also a lipid droplet fluorescent probe.²² Its targeted imaging ability has been demonstrated in a variety of assays.

Aggregation-induced emission luminogens (AIEgens)²³ are also widely used as biosensors and for disease diagnostic studies due to their excellent aggregated-state luminescence enhancement properties. However, such fluorescent probes usually require an exogenous light source for excitation and may not be as suitable for atherosclerosis treatment in practical applications.

To address the limitations of external light-dependent PDT, chemiluminescence-based strategies have emerged as a promising alternative. Chemiluminescence is based on the interaction of different chemical compositions to produce an illuminant that can replace the external excitation light to excite the photosensitizers. Ding et al. synthesized a self-luminescent nanomaterial containing bis(2,4,5-trichloro-6-[pentyloxycarbonyl]phenyl)oxalate (BTPO) for tumor therapy.²⁴ BTPO excites photosensitizers at the lesion site and generates ¹O₂, which induces apoptosis and inhibits the proliferation of tumor cells. ¹O₂ can induce apoptosis and inhibit the proliferation of tumor cells. This PDT shows excellent application prospects. Meanwhile, it also provides a novel idea for the treatment of AS.

Here, we report the development of platelet membrane (PM)-coated PLGA nanoparticles encapsulating chlorin e6 (Ce6) and BTPO (PM@CBNP), which leverages plaque-targeting and self-illuminating properties to enable efficient PDT in AS. In this study, platelet membrane (PM)-modified PLGA nanoparticles encapsulating chlorin e6 (Ce6) and BTPO (PM@CBNP) were prepared (Scheme 1). PM have a high affinity for vulnerable plaques: (1) adhesion proteins on

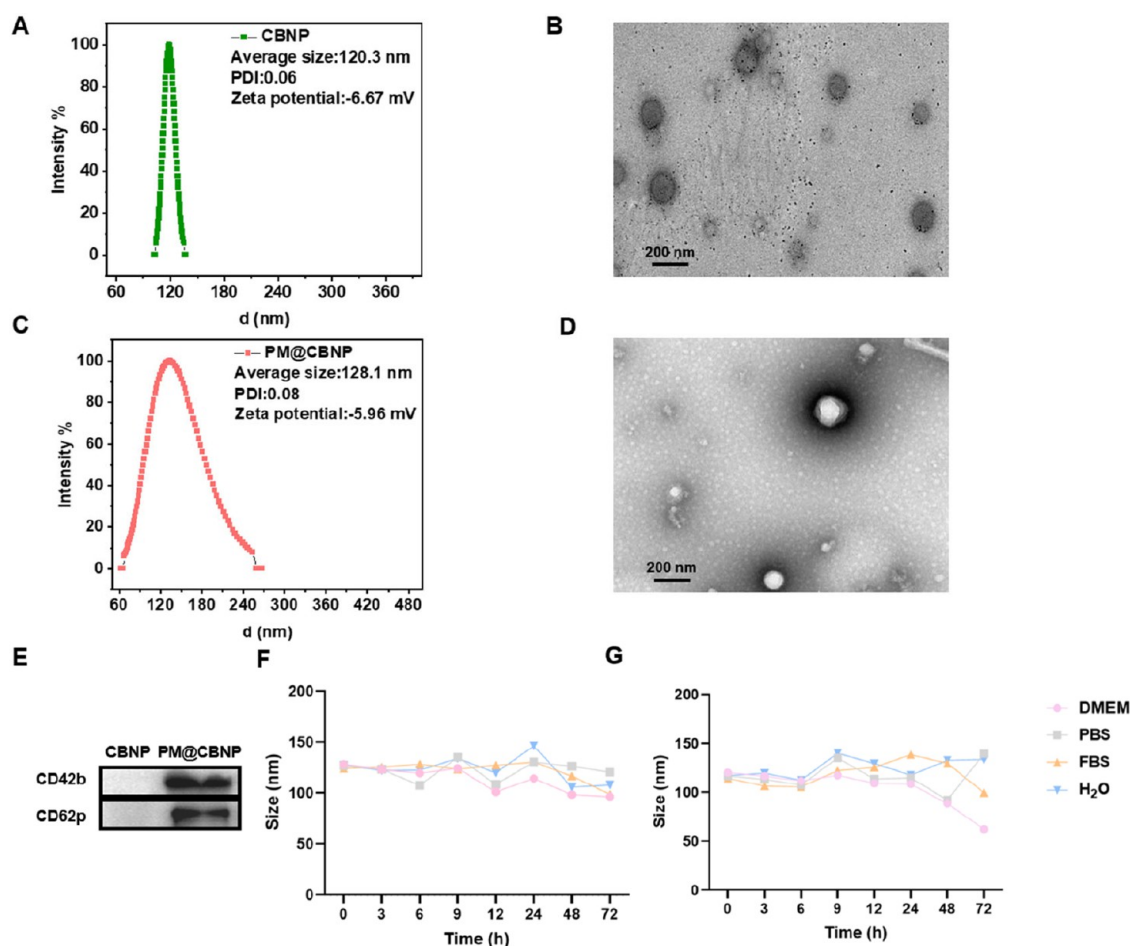


Figure 1. Characterization and functional verification of CBNP and PM@CBNP. (A) Size distribution and (B) morphology of the CBNP. (C) Size distribution and (D) morphology of PM@CBNP. (E) Western blotting to detect the expression of CD42b and CD62p. (F) Sizes of PM@CBNP and (G) CBNP in different media within 72 h. Scale bar: 200 nm. * $p < 0.05$, ** $p < 0.01$, *** $p < 0.001$ and **** $p < 0.0001$. n.s.: not significant. Error bar: mean \pm SD.

the surface of the platelet membrane, such as the GP Ib-IX complex, are able to bind to collagen or von Willebrand (vW) factor exposed at the rupture of the plaque. (2) Platelet membranes mimic the chemotaxis of natural platelets and are attracted to the plaque site by inflammatory factors. Thus, the modification of PM achieves the targeting of PM@CBNP. Due to the presence of large amounts of H₂O₂ in the plaque microenvironment, chemiluminescence occurs to excite Ce6, allowing for ¹O₂ production. This also overcomes the limitation that external excitation light does not penetrate deeply enough to reach the lesion site. Meanwhile, due to the unique targeting ability of PM to the plaque, chemiluminescence PDT based on PM@CBNP specifically stimulates the apoptotic process²⁵ in the vulnerable plaque without damage to normal tissues.

RESULTS AND DISCUSSION

Characterization of PM@CBNP. The nanoparticles in this study can generate a chemiluminescent reaction in a H₂O₂ microenvironment and induce ¹O₂ generation for atherosclerosis therapy. PM@CBNP were prepared. PM@CBNP are capable of generating ¹O₂ in the presence of H₂O₂ without light irradiation.

CBNP exhibited a near-spherical morphology with an average diameter of approximately 120.3 nm (Figure 1A).

When the PM was modified on the surface of CBNP, PM@CBNP were obtained. The average diameter of PM@CBNP was 128.1 nm (Figure 1B). CBNP and PM@CBNP exhibited uniform size distribution and spherical morphology (Figure 1C,D).

By TEM, it can be found that there was an obvious difference between CBNP and PM@CBNP in terms of appearance. Meanwhile, the average diameter of PM@CBNP was larger than that of CBNP, indicating successful coating of PM. Meanwhile, the marker proteins of platelets (CD42b and CD62p) were detected in the PM@CBNP group (Figure 1E). This also demonstrated that the PM was successfully modified on the surface of CBNP. At the same time, XPS detection results (Figures S1 and S2) showed that PM@CBNP had significant membrane protein characteristic peaks, especially N 1s, S 2p, and P 2p peaks. This result further confirmed that the PM was successfully modified on the CBNP surface.

In order to verify the stability of PM@CBNP, PM@CBNP were placed in four different solutions, and their changes were observed within 2 weeks (Figure S3). The size distribution of nanoparticles was stable at about 6 h (Figure 1F,G). Except for CBNP in water and PBS, the size of nanoparticles in other media decreased in 9–72 h. Specifically, in the case of DMEM, after 72 h, the diameters of CBNP and PM@CBNP were 62.4 and 96.3 nm, respectively. Additionally, the results showed that

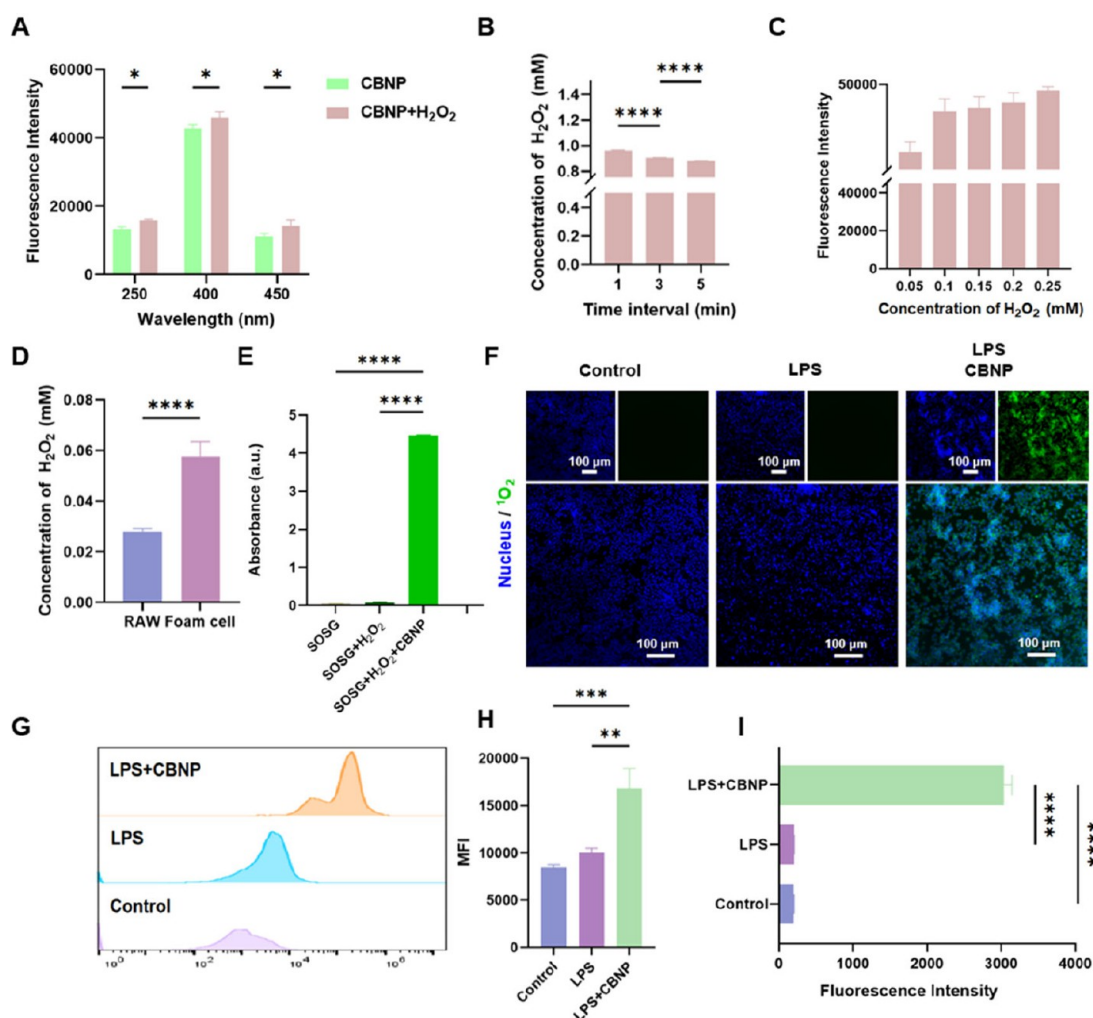


Figure 2. CBNP promote generation of $^1\text{O}_2$. (A) Fluorescence intensity of free CBNP versus that of CBNP treated with H_2O_2 . (B) Change in the H_2O_2 concentration within 5 min after mixing CBNP with H_2O_2 . (C) Fluorescence intensity of H_2O_2 mixed with CBNP at concentrations of 0.05, 0.1, 0.15, 0.2, and 0.25 mM. (D) H_2O_2 concentrations of RAW264.7 and RAW264.7 were activated by LPS. (E) Verification of $^1\text{O}_2$ generation, $^1\text{O}_2$ labeled with SOSG. (F) CLSM observation of $^1\text{O}_2$ expression and (I) quantitative analysis in RAW264.7 activated by LPS after treatment with CBNP. Nucleus was stained with DAPI (blue), and $^1\text{O}_2$ was labeled with SOSG (green). Scale bar: 100 μm . (G) Flow cytometry image and (H) quantitative analysis of intracellular $^1\text{O}_2$ in activated RAW264.7 pretreated with LPS and incubated with CBNP. Scale bar: 100 μm . * $p < 0.05$, ** $p < 0.01$, *** $p < 0.001$ and **** $p < 0.0001$. n.s.: not significant. Error bar: mean \pm SD.

after 24 h, the particle size of CBNP decreased significantly in both FBS and DMEM environments. We speculate that this is due to the presence of esterases in both environments, which accelerate ester bond hydrolysis, leading to particle disintegration. In contrast, PM@CBNP, which possess a natural lipid bilayer structure provided by platelet membranes, exhibit enhanced steric hindrance and electrostatic repulsion due to surface glycoproteins (e.g., CD47) and negative charges (sialic acid).

Validation of Chemiluminescence and $^1\text{O}_2$ Production. To demonstrate that BTPO undergoes chemiluminescence in a H_2O_2 environment, the fluorescence intensity produced by Ce6 in CBNP-containing BTPO was measured. In order to avoid the excitation of Ce6 by an external light, CBNP were placed under non-Ce6 excitation wavelengths. The fluorescence intensity of Ce6 was significantly stronger in the presence of H_2O_2 than in a H_2O_2 -free environment (Figure 2A). Specifically, at different excitation wavelengths, the fluorescence intensities of CBNP + H_2O_2 were enhanced by 19.9, 7.6, and 27.1%, respectively, compared with those of the

CBNP group. BTPO in CBNP itself does not emit light but can undergo a chemiluminescence reaction in the presence of H_2O_2 , resulting in fluorescence. Therefore, the fluorescence of CBNP + H_2O_2 is significantly enhanced. Meanwhile, in another experiment, CBNP were placed in H_2O_2 , and the changes of H_2O_2 concentration were measured every 2 min. It was found that the concentration of H_2O_2 decreased significantly (Figure 2B) over time. Within 3 min, the fluorescence intensity decreased by 5.8% from the initial level and by 8.2% in 5 min. This proves that H_2O_2 is indeed involved in the chemiluminescence process.

In addition, the relationship between the H_2O_2 concentration and the intensity of chemiluminescence was investigated. The fluorescence intensity increased with the increase of the H_2O_2 concentration (Figure 2C). RAW264.7 was activated with LPS to mimic foam cells in the plaque. More H_2O_2 was produced in the foam cells (Figure 2D) compared to normal RAW264.7. It provides a favorable environment for chemiluminescence at the plaque.

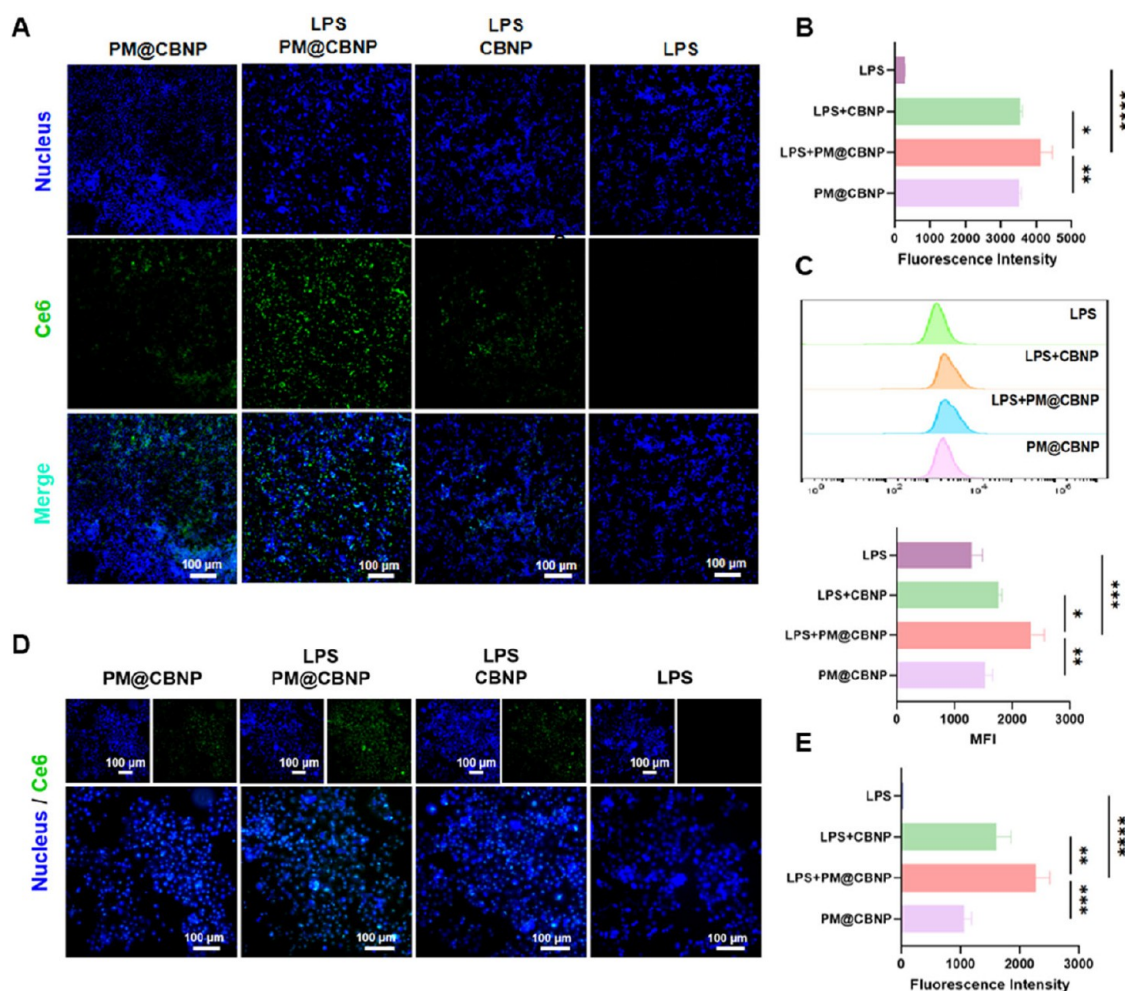


Figure 3. Targeting of RAW264.7 and HUVEC by CBNP and PM@CBNP. (A) Confocal images and (B) quantitative analysis of RAW264.7 after treatment with CBNP and PM@CBNP. (C) Flow cytometry results and quantitative analysis of intracellular Ce6 in activated RAW264.7 pretreated with LPS or normal RAW264.7 incubated with CBNP and PM@CBNP. (D) Confocal images and (E) quantitative analysis of HUVEC after treatment with CBNP and PM@CBNP. Scale bar: 100 μm . * $p < 0.05$, ** $p < 0.01$, *** $p < 0.001$ and **** $p < 0.0001$. n.s.: not significant. Error bar: mean \pm SD.

$^1\text{O}_2$ is a kind of highly reactive free radical.^{26,27} $^1\text{O}_2$ can damage various intracellular components (DNA, RNA, lipids, and proteins) and induce apoptosis or necrosis.

Therefore, $^1\text{O}_2$ produced by the reaction of Ce6 with oxygen could induce the apoptosis of macrophages at the plaque. Moreover, $^1\text{O}_2$ could alleviate the progression of atherosclerosis. The generation of $^1\text{O}_2$ was quantified by the fluorescent probe SOSG. SOSG emitted green fluorescence in H_2O_2 in the presence of CBNP. This indicated that a large amount of $^1\text{O}_2$ was generated in the mixture. BTPO in nanoparticles undergoes a chemiluminescence reaction in a H_2O_2 environment (Figure 2E). At the same time, we indirectly determined the $^1\text{O}_2$ quantum yield²⁸ of CBNP to be 0.74 using chemiluminescence (Figure S4). CBNP exhibit good photodynamic effects.

Meanwhile, to verify $^1\text{O}_2$ production more visually, RAW264.7 activated with LPS was cocultured with CBNP in another experiment. CLSM showed that SOSG fluorescence intensity was significantly enhanced (Figure 2F,I) when CBNP was in the inflammatory microenvironment. Specifically, fluorescence intensity of the cells treated with CBNP in the presence of H_2O_2 showed a 15-fold increase compared with that of the control group (PBS treatment).

In flow cytometry (Figure 2G,H), the same results could be observed. MFI in the CBNP group increased by 50.0 and 40.4%, respectively, compared to the control and LPS groups.

These results suggest that BTPO in the CBNP can spontaneously generate light sufficient to excite Ce6 in an intraplaque H_2O_2 environment, while Ce6 generates $^1\text{O}_2$ in response to the environment.

Targeting Ability of PM@CBNP In Vitro. PM proteins have very strong affinity for plaques, mainly due to the presence of damaged endothelial cells and exposed collagen on the surface of fragile plaques, as well as monocyte-platelet aggregates (MPAs) produced through the interaction of P-selectin glycoprotein ligand-1 (PSGL-1) with P-selectin.^{29–33} Based on this phenomenon, it is believed that the PM has a strong binding affinity for plaques and can bind damaged endothelial cells with macrophage-derived foam cells. In this section, the uptake of PM@CBNP by activated RAW264.7 (Figure 3A) and activated HUVEC was evaluated (Figure 3D).

Compared to CBNP (platelet membrane-free), PM@CBNP were more likely to bind to activated RAW264.7 and HUVEC. The fluorescence intensity of PM@CBNP (Figure 3B) in activated RAW264.7 and HUVEC was 1.2 and 1.7 times that of CBNP, respectively. Meanwhile, the MFI of PM@CBNP in

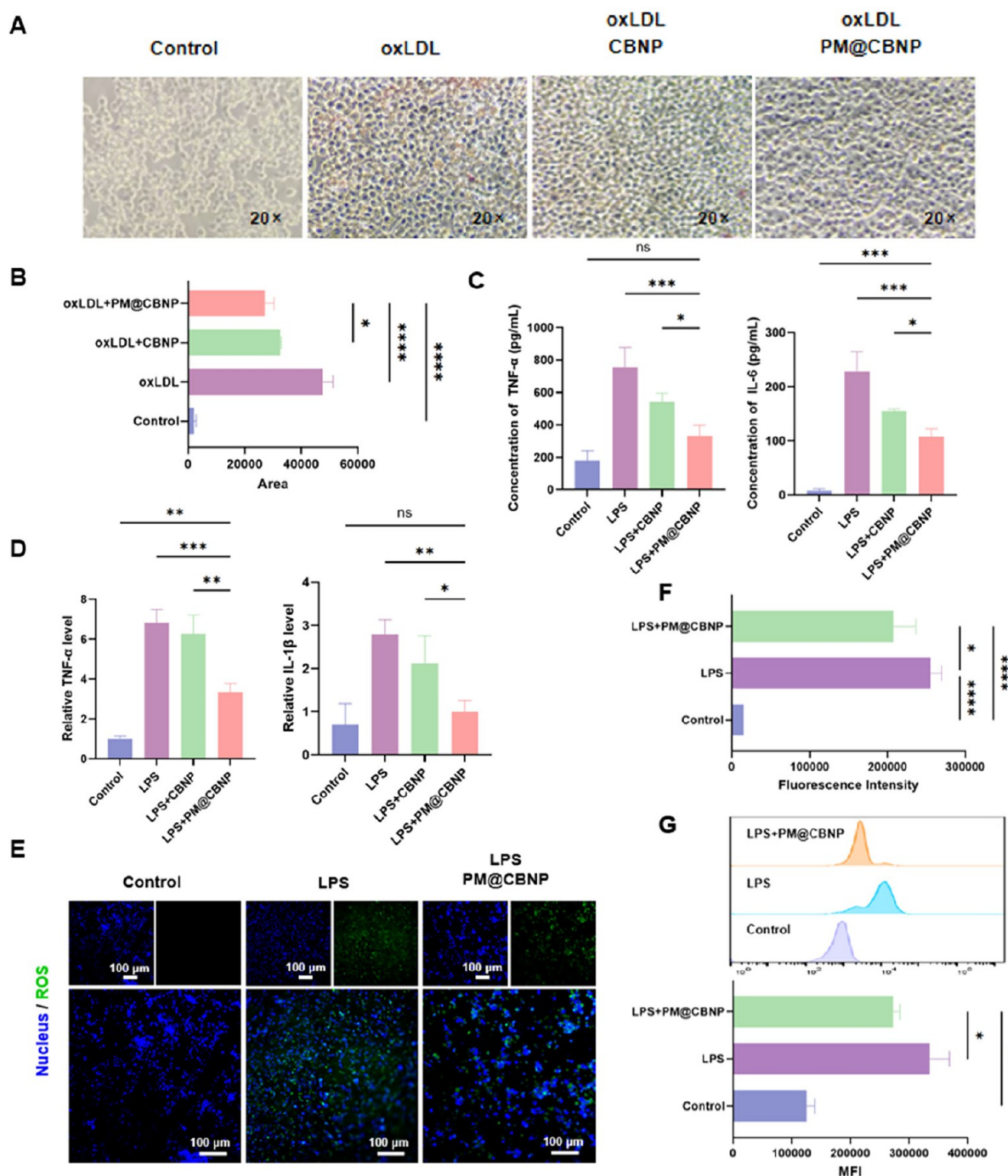


Figure 4. PM@CBNP reduce lipids and inflammatory factors. (A) Representative images and (B) quantification of Oil Red O (ORO) staining of RAW264.7 treated with CBNP and PM@CBNP. (C) Expression of IL-6 and TNF-α of activated RAW264.7 cells treated with CBNP and PM@CBNP. (D) Relative expression of TNF-α and IL-1β produced by activated RAW264.7 cells treated with CBNP ($n = 3$) and PM@CBNP ($n = 3$) as measured by qPCR. (E) CLSM observation of ROS expression and (F) quantitative analysis in RAW264.7 activated by LPS after treatment with PM@CBNP. Nucleus was stained with DAPI (blue), ROS was labeled with DCFH-DA (green). (G) Flow cytometry results and quantitative analysis of intracellular ROS in activated RAW264.7 pretreated with LPS and incubated with CBNP. Scale bar: 100 μm. * $p < 0.05$, ** $p < 0.01$, *** $p < 0.001$, and **** $p < 0.0001$. n.s.: not significant. Error bar: mean \pm SD.

activated RAW264.7 and HUVEC was 1.2 times and 3.1 times (Figure 3B,E) than nonactivated cells. The results from flow cytometry (Figure 3C) also support the above findings. The uptake of PM@CBNP by activated RAW264.7 was 1.5 times that of normal RAW264.7. At the same time, the uptake rate of activated RAW264.7 to PM@CBNP was 1.3 times that of CBNP. These results suggest that, compared to CBNP, PM@

CBNP can more effectively target damaged endothelial cells and foam cells.

At the same time, it could be found that in both RAW 264.7 and HUVEC, the activated RAW 264.7 seemed to bind more PM@CBNP. The fluorescence intensity of PM@CBNP in activated RAW 264.7 was 1.8 times that of HUVEC. This result suggests that PM@CBNP appear to have a higher affinity for foam cells. This demonstrates that platelets

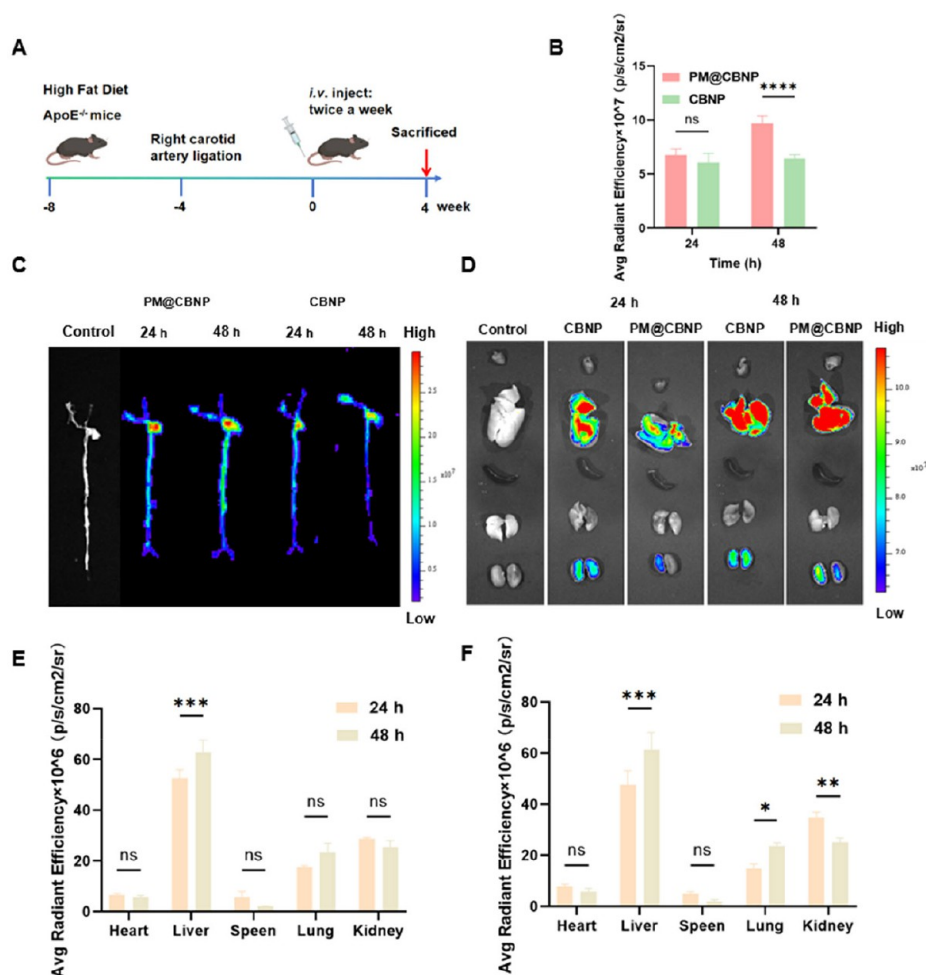


Figure 5. PM@CBNP target the aortic arch and reduce plaque burden. (A) Timeline diagram of the animal experiment. (C) Representative ex vivo images and (B) fluorescent intensity of aortas with plaques from ApoE^{-/-} mice treated with CBNP ($n = 3$) and PM@CBNP ($n = 3$) at different time points. (D) Representative ex vivo images and fluorescence intensity of major organs (heart, liver, spleen, lung, and kidney) from mice treated with (E) CBNP and (F) PM@CBNP. * $p < 0.05$, ** $p < 0.01$, *** $p < 0.001$ and **** $p < 0.0001$. n.s.: not significant. Error bar: mean \pm SD.

preferentially accumulate in damaged endothelial and vulnerable plaques.

To determine whether the targeting of PM@CBNP depends on the function of the GP Ib-IX complex and vW factor, fucoidan was used as an inhibitor of the GP Ib-IX complex and the vW factor,³⁴ and cells were pretreated with it. The results (Figure S5) showed that after fucoidan intervention, the fluorescence intensity of PM@CBNP decreased significantly. Meanwhile, the fluorescence intensity of CBNP did not show significant changes before and after treatment. This indicates that PM@CBNP primarily enter cells via the GP Ib-IX complex and the vW factor. Specifically, after the endocytic pathway was blocked, the fluorescence intensity of PM@CBNP decreased by 93.1 and 93.4% in RAW264.7 and HUVEC, respectively.

In Vitro Therapeutic Efficacy. According to the molecular mechanism of atherosclerosis, macrophages are apt to engulf excess lipids to form foam cells,³⁵ which produce ROS and recruit inflammatory factors.^{36–43} PM@CBNP and CBNP inhibited the accumulation of lipid droplets in RAW264.7 activated by ox-LDL (Figure 4A). Specifically, compared with the ox-LDL group, the inhibition rates of PM@CBNP and CBNP were 42.8 and 31.8%, respectively (Figure 4B).

Similarly, PM@CBNP and CBNP inhibited inflammatory factors by detecting the levels of inflammatory factors TNF- α and IL-1 β by ELISA (Figure 4C). PM@CBNP eliminated 52.9% of IL-6 and 56.0% of TNF- α compared with the LPS group. Similar results can be obtained from qPCR (Figure 4D). After PM@CBNP treatment, TNF- α and IL-1 β expression decreased by 50.1 and 64.4%, respectively, compared with that of the LPS group.

The presence of high levels of ROS in atherosclerotic plaques causes mass cell apoptosis, which can lead to increased plaque vulnerability. In order to verify the effect of PM@CBNP on ROS levels, ROS was labeled by the DCFH-DA probe and observed by a confocal microscope (Figure 4E). The clearance rate of PM@CBNP was 18.7% compared with the LPS group (Figure 4F). The results of flow cytometry (Figure 4G) were similar. The MFI of ROS of the PM@CBNP group decreased by 18.4% compared with the LPS group. It can be hypothesized that PM@CBNP do not have a notable effect on ROS removal due to the production of ¹O₂. However, the overall ROS content was still reduced due to the consumption of H₂O₂. Reduced ROS levels delay plaque formation and deterioration.

The foam cells in the plaque produce inflammatory cytokines that promote inflammation in the plaque, thus

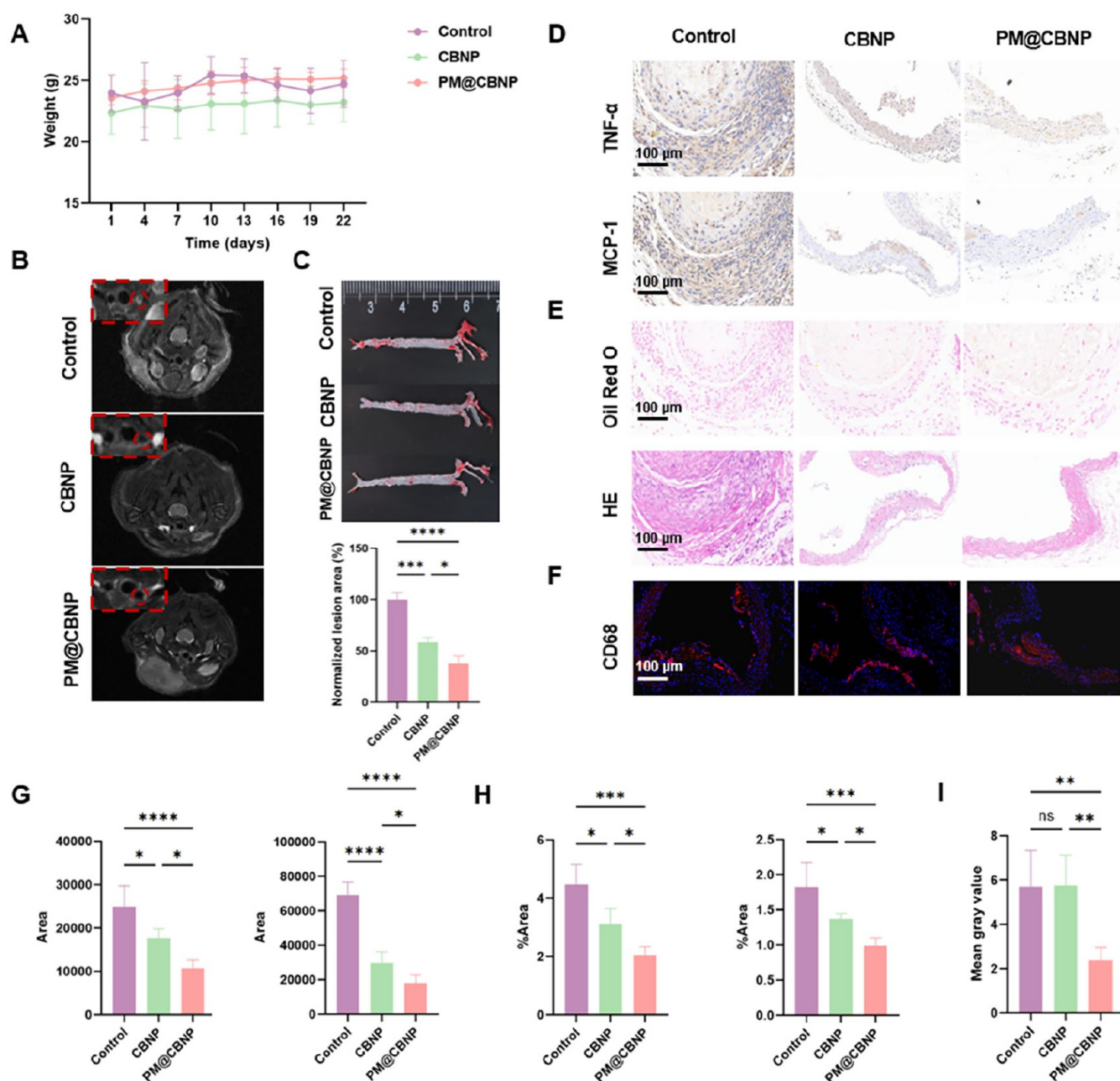


Figure 6. PM@CBNP reduce inflammatory expression at the aortic arch and alleviate atherosclerosis. (A) Changes of body weights of mice during different treatments. (B) MRI of the cross-section of carotid arteries in vivo. (C) Representative images ORO-stained aortas and quantitative analysis from mice treated with CBNP ($n = 3$) and PM@CBNP ($n = 3$). (D) Representative images after immunohistochemistry staining of the aortic root sections with TNF- α and MCP-1 and (G) quantitative analysis ($n = 6$). (E) Representative images of Oil Red O-stained sections and H&E staining of plaque areas in aortic roots for mice and (H) quantitative analysis ($n = 6$). (F) Immunofluorescence images of double staining for CD68 to label macrophages and (I) quantitative analysis ($n = 6$). Scale bar: 100 μm . * $p < 0.05$, ** $p < 0.01$, *** $p < 0.001$ and **** $p < 0.0001$. n.s.: not significant. Error bar: mean \pm SD.

exacerbating the lesion. PM@CBNP can inhibit the formation of inflammatory factors by inhibiting the ROS and producing $^1\text{O}_2$, which can scavenge foam cells. Therefore, PM@CBNP play a role in alleviating the early atherosclerotic lesions.

However, there is a question: how does $^1\text{O}_2$ scavenge cells? We reviewed the paper for cell death triggered by photodynamic therapy, which usually includes the forms of pyroptosis and apoptosis. In the experiments of Li et al.,⁴⁴ a photosensitizer loaded with ce6 induced pyroptosis in macrophages. In the experiments of Hu et al.,⁴⁵ photodynamic therapy induced apoptosis by activating caspase-3. It is also

possible that apoptosis and pyroptosis act simultaneously. In order to clarify the mechanism by which $^1\text{O}_2$ plays a role in cellular clearance, we performed the validation of both pyroptosis and apoptosis.

Pyroptosis is an inflammatory form of programmed cell death that depends on the activation of the gasdermin protein family to induce cell membrane perforation, leading to the leakage of cellular contents, particularly large amounts of inflammatory factors (e.g., IL-18 and IL-1 β), thereby triggering an inflammatory response. Lactate dehydrogenase (LDH) is an enzyme that is normally present within cells. During pyroptosis

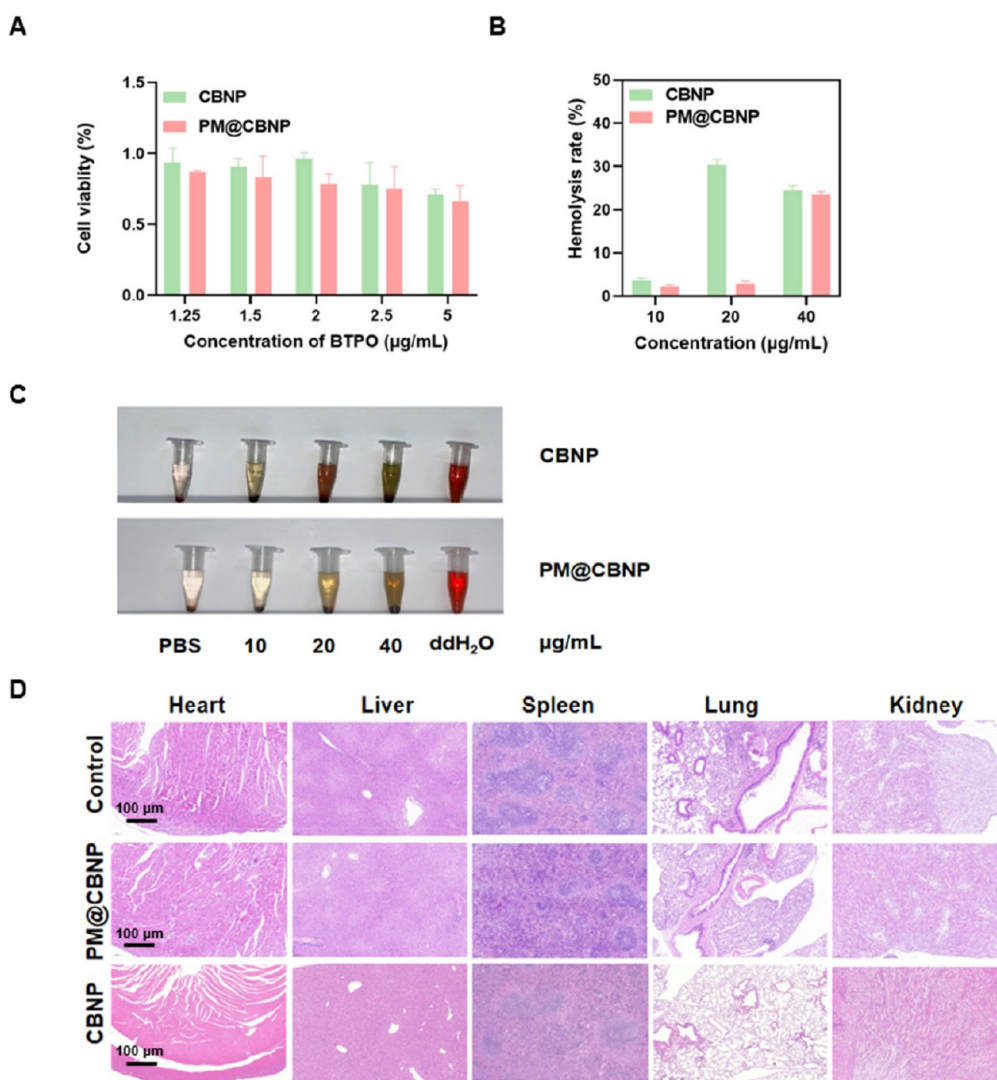


Figure 7. Biosafety validation of the PM@CBNP. (A) Cell viability of RAW264.7 pretreated with LPS (1 μg/mL) and incubated with CBNP and PM@CBNP at different concentrations. (B) Hemolysis rate and (C) images of CBNP and PM@CBNP with different concentrations. (D) Histological changes evaluated by H&E staining in atherosclerotic mice treated with CBNP and PM@CBNP.

(or any stimulus causing cell membrane rupture), LDH is released through the ruptured cell membrane.

LDH results (Figure S6C) revealed that the LDH release rate was significantly elevated in the PM@CBNP group compared to that in the control group. This suggests that PM@CBNP may promote pyroptosis. However, interestingly, there were no significant differences between LPS, PM@CBNP, and LPS+PM@CBNP. This may indicate that PM@CBNP do not significantly promote pyroptosis in an inflammatory environment.

The WB results (Figure S6A,B) showed that PM@CBNP increased the protein expression of GSDMD-N in an inflammatory environment. Combining the results of LDH and IL-1β, we speculate that PM@CBNP may promote pyroptosis, but not significantly.

Additionally, there were significant changes in Caspase-3, Bax, and Bcl-2 (Figure S6D,E), which are key proteins in apoptosis. The results show that PM@CBNP increased the protein expression levels of Caspase-3 and Bax, while the expression level of Bcl-2 decreased. Furthermore, the results indicate that, compared to the control group, PM@CBNP do not significantly promote apoptosis under normal conditions.

However, PM@CBNP significantly promotes apoptosis under inflammatory conditions. This suggests that PM@CBNP primarily clears inflammatory macrophages by promoting apoptosis.

AS Plaques Targeting and Therapeutic Efficacy of PM@CBNP In Vivo. Atherosclerotic plaques were easily formed in apolipoprotein E-deficient (ApoE^{-/-}) mice after long-term feeding of the high-fat diet (Figure 5A). Ce6 itself has certain fluorescence characteristics and can produce strong fluorescence. Therefore, the targeting of PM@CBNP in vivo can be detected by fluorescence imaging. In this experiment, saline (control group), PM@CBNP, and CBNP were injected into atherosclerotic mice. The mice were executed 24 and 48 h after injection, and the aortas were collected and observed by IVIS Spectrum.

The fluorescence of Ce6 is visible over a large area. More importantly, the aorta treated with PM@CBNP showed stronger fluorescence than the aorta treated with CBNP (Figure 5C). Moreover, the fluorescence intensity in the aortic arch was significantly stronger than that in the rest of the aorta because plaque was more likely to form there.

These results suggest that PM@CBNP showed a stronger affinity for plaque. Furthermore, our previous studies¹⁹ have not been explored for targeting ability.

After 48 h of injection, the fluorescence intensity of the PM@CBNP group was 1.5 times that of the CBNP group (Figure 5B). In addition, imaging results (Figure 5D) showed that PM@CBNP was predominantly metabolized through the liver and kidney (Figure 5E,F).

In Vivo Therapeutic Efficacy. In order to explore the antiatherosclerosis effect of PM@CBNP, ApoE^{-/-} mice with atherosclerosis were randomly divided into three groups, which were injected with saline (control group), PM@CBNP, and CBNP via the caudal vein twice a week for 4 weeks.

Over the time of treatment, there were no significant weight changes in both PM@CBNP and CBNP groups (Figure 6A). T2MRI results showed that right carotid stenosis was significantly lower in the PM@CBNP and CBNP groups, compared with the control group. More importantly, the right carotid artery (Figure 6B) of the PM@CBNP group was significantly larger than that of the CBNP group. PM@CBNP were more effective than CBNP in treating plaque.

After treatment, the plaque area was obviously reduced (Figure 6C). Specifically, the PM@CBNP and CBNP groups showed a decrease in the lesion area of 62.3 and 41.4% compared to the control group.

The expression of TNF- α and MCP-1 in the aorta decreased significantly after treatment (Figure 6D). Specifically, PM@CBNP and CBNP groups decreased by 57.4, 73.8, and 29.2, 57.1%, respectively (Figure 6G). PM@CBNP and CBNP significantly reduced the lesion area, and PM@CBNP showed better therapeutic effect compared with CBNP. Specifically, PM@CBNP and CBNP are 54.3 and 30.1% less integrated, respectively (Figure 6E,H).

The decreased expression of CD68 indicated apoptosis (Figure 6F) in PM@CBNP and CBNP plaques. Compared with the control group, the expression of CD68 decreased by 58.4% in the PM@CBNP group (Figure 6I). These results suggest that PM@CBNP could reduce the expression of plaque accumulation and inflammation and relieve the burden of atherosclerosis. The results of H&E staining (Figure 6E,H) support the above conclusion.

The in vivo therapeutic effects of PM@CBNP are focused on the ApoE^{-/-} mouse model. Previous studies have shown that plaques in ApoE mice are richer in inflammatory cells and necrotic cores,⁴⁶ while lesions in LDLR mice induced by an HFD are more similar to human late-stage plaques.⁴⁷ Therefore, PM@CBNP may be more suitable for atherosclerosis induced in ApoE mice, while its efficacy in LDL-C-dominated pathology requires further validation. Future work could be extended to LDLR models or ApoE/LDLR double-knockout mice to assess whether "PM@CBNP photodynamic therapy" is equally effective in LDL-C-dependent atherosclerosis. Additionally, the combination of humanized mice (such as ApoE3-Leiden) may enhance clinical translational significance.

Biosafety Analysis of PM@CBNP In Vivo and In Vitro. Finally, biosafety is another aspect that needs to be examined. Cell viability was calculated by eq 1. Cells reached half lethal at 10 and 20 $\mu\text{g/mL}$ in PM@CBNP and CBNP, respectively. High activity was observed at 1.25 $\mu\text{g/mL}$. Interestingly, PM@CBNP seemed to scavenge more cells (Figure 7A) than CBNP at the same concentration of BTPO. Specifically, at different concentrations, compared to CBNP, PM@CBNP increased

the inhibition rate of activated RAW264.7 by 4.6, 8.1, 22.8, 3.3, and 6.1%. This may also explain why PM@CBNP is more effective than CBNP in therapy.

When the hemolysis rate is less than 5%, the drug is considered to be biosafe. The hemolysis rate was calculated using eq 2. The hemolysis rates of PM@CBNP and CBNP were 1.8 and 3.2%, respectively, when the concentration of BTPO was 10 $\mu\text{g/mL}$, showing high safety (Figure 7B,C). However, when the concentration increased to 20 $\mu\text{g/mL}$, only PM@CBNP showed safety. These results indicate that PM@CBNP have higher biosafety than CBNP. At the same time, through blood biochemical parameters and others (Figure S7, Tables S1, and S2), it can also be observed that after treatment, the inflammation in the mice was alleviated, and no other abnormalities were exhibited. Similarly, H&E staining of the main organs (Figure 7D) of atherosclerotic mice showed that PM@CBNP had good biological safety.

CONCLUSIONS

In conclusion, PM@CBNP can target plaques, activate Ce6 in the presence of H₂O₂, and generate ¹O₂. This novel PDT can reduce the inflammatory response within the plaque and alleviate the development of atherosclerosis.

EXPERIMENTAL SECTION

Materials. Bis{3,4,6-trichloro-2-[(pentyloxy)carbonyl]phenyl} oxalate (BTPO) was provided by Shanghai Macklin Biochemical Co., Ltd. Ce6 was purchased from MedChemExpress (Shanghai). Lipopolysaccharide (LPS) and 2',7'-dichlorodihydrofluorescein diacetate (DCFH-DA) were supplied by Shanghai Macklin Biochemical Co., Ltd. Cell Counting Kit-8 (CCK-8), Hydrogen Peroxide (H₂O₂) Assay Kit, Modified Oil Red O Staining Kit, Singlet Oxygen Sensor Green Fluorescent Probe (SOSG), LDH assay kit, and 2-(4-amidinophenyl)-6-indolecarbamidine dihydrochloride (DAPI) were purchased from Beyotime Biotechnology (Shanghai, China). Oxidized low-density lipoprotein (ox-LDL) was obtained from Guangzhou Yiyuan Biotechnology Co., Ltd. Antibodies were purchased from Proteintech. Six-week-old C57BL/6 mice and ApoE^{-/-} mice were provided by the Model Animal Research Center of Nanjing University.

CBNP Preparation. Eleven mg of PLGA, Ce6, and BTPO were dissolved in 1.2 mL of DCM/DMSO (5/1, v/v) with the mass ratio of 20/1/1 and ultrasonically solubilized for 10–30 min away from light. Then, 50 mg of PVA was weighed and added to 10 mL of ddH₂O, heated, and stirred until dissolved. The two solutions were mixed and emulsified by ultrasonication (20 kHz, 10 s on, 3 s off, 10–20 min) in an ice bath until translucent. The sonicated mixture was stirred overnight away from light to induce volatilization of DCM. The final solution obtained was CBNP.

PM@CBNP Preparation. Whole blood was collected in an anticoagulant tube from C57BL/6 mice (Model Animal Research Center of Nanjing University). It was centrifuged at 850 $\times g$ for 10 min at 4 $^{\circ}\text{C}$, the supernatant was discarded, and the precipitate was resuspended in saline. After repeated centrifugation and washing 3 times, the samples were resuspended in saline containing protease inhibitors, frozen in liquid nitrogen, thawed at 37 $^{\circ}\text{C}$, and repeated 3–4 times. The sample was centrifuged at 4000 $\times g$ for 5 min at 4 $^{\circ}\text{C}$, and the supernatant was discarded. The precipitate was resuspended in saline containing protease inhibitors and washed by repeated centrifugation 3 times to obtain the PM. The PM was quantified to the corresponding concentration with saline containing protease inhibitors.

The quantified PM was mixed with CBNP and sonicated for 15–30 min away from light until the solution was clear. The final solution obtained was PM@CBNP.

Chemiluminescence Imaging of CBNP. To verify whether the reaction of BTPO and H₂O₂ can produce endogenous excitation light,

CBNP were excited at a non-Ce6 excitation wavelength, the emission wavelength was fixed, and the fluorescence intensity was detected, which was compared with that without H₂O₂. In another experiment, the nanoparticles were colocalized with a certain initial concentration of H₂O₂, and the concentration of H₂O₂ was detected after different time intervals. In order to investigate the link between H₂O₂ concentration and fluorescence intensity, the nanoparticles were placed in different concentrations of H₂O₂ and detected for fluorescence intensity and absorbance (Tecan Spark, Nanodrop one).

Detection of ¹O₂ in Nanoparticles. To verify the successful production of ¹O₂ by Ce6 after chemiluminescence, the ¹O₂ fluorescent probe SOSG was added to the mixture, and the change in absorbance was detected (Nanodrop one).

Determination of H₂O₂ Content. RAW264.7 were inoculated in six-well plates and activated by LPS (1 μg/mL) or ox-LDL (80 μg/mL) for 24 h. H₂O₂ content was determined by reference to the H₂O₂ Content Assay Kit.

Determination of ¹O₂ Production. Cells were inoculated in six-well plate cell crawler slices (3 × 10⁵ cells per well) and incubated overnight. Cells were treated with PBS, LPS, and LPS+CBNP. The concentrations of LPS and CBNP were set as 1 and 1.25 μg/mL, respectively. After 24 h of incubation, the culture medium was replaced with fresh medium containing SOSG (5 μM). After 1 h, cells were collected for analysis by flow cytometry. Cells were washed 3 times and fixed by 4% PFA for 15 min. After the nucleus was stained with DAPI for 5 min, cells were washed 3 times. Cell crawls were picked out with forceps and placed face down on a slide with a drop of a sealing solution. Cells were photographed by CLSM.

Cellular Targeting of CBNP and PM@CBNP. Cells were inoculated in six-well plates crawls (3 × 10⁵ cells per well) and treated with PM@CBNP (1.25 μg/mL), LPS+PM@CBNP, LPS+CBNP (1.25 μg/mL), and LPS (1 μg/mL). After incubation with nanoparticles for 6 h, the cells were washed with PBS, fixed with 4% PFA, and stained with DAPI, and fluorescent images were taken. HUVEC also performed the experiment as above.

In another experiment, cells were collected after co-incubation with CBNP and PM@CBNP, washed by PBS, and detected by flow cytometry (BD Accuri C6 Plus).

Changes in ROS Expression Levels after Treatment. Cells were inoculated in six-well plate crawls (3 × 10⁵ cells per well) and treated with PBS, LPS (1 μg/mL), and LPS+CBNP (1.25 μg/mL). After 6 h, the culture medium of the cells in the three groups was discarded, and the cells were stained with DCFH-DA and DAPI. Cells were washed, fixed, and photographed by CLSM.

In another experiment, cells were collected after co-incubation with CBNP, stained with DCFH-DA, washed, and detected by flow cytometry (BD Accuri C6 Plus).

Expression Levels of Foam Cell-Associated Inflammation after Treatment. Cells were inoculated in six-well plates and treated with PBS, CBNP, and PM@CBNP after activated. The cellular RNA level was extracted for qPCR (QuantStudio5).

Changes in Intracellular Lipid Levels after Treatment. RAW264.7 were seeded in six-well plates (3 × 10⁵ cells per well) and treated with PBS, ox-LDL (80 μg/mL), ox-LDL+CBNP (1.25 μg/mL), and ox-LDL+PM@CBNP (1.25 μg/mL). The culture medium in the wells of each group was discarded, washed with PBS, and fixed with 4% PFA for 10 min after PBS was rinsed; the staining wash solution was added and incubated for 20 s. The wash solution was discarded, and the oil red staining solution was added and incubated for 30 min away from light. After staining was completed, the cells were rinsed with the staining wash solution and observed with an inverted microscope.

Cell Viability Assays. RAW264.7 cells were seeded into 96-well plates (8000 cells per well, five wells for each group, with DMEM as the culture medium) and incubated overnight for cell adherence. The next day, DMEM was removed, and the cells were washed twice with PBS. Then, 100 μL DMEM containing CBNP and PM@CNP with different BTPO concentrations (1.25, 2, 5, 10, and 20 μg/mL) was added to each well. The plates were then incubated at 37 °C for 24 h. After incubation, 10 μL of a CCK-8 solution was added. After

incubation for 1 h at 37 °C, cell viability was evaluated by the absorbance at 450 nm measured on a microplate reader. Cell viability (%) was determined as follows:

$$\text{Cell viability\%} = \frac{\text{OD}_{\text{sample}} - \text{OD}_{\text{blank}}}{\text{OD}_{\text{control}} - \text{OD}_{\text{blank}}} \times 100\% \quad (1)$$

In another experiment, RAW264.7 were activated by LPS or ox-LDL overnight. Then, CBNP and PM@CBNP with different concentrations (1.25, 1.5, 2, 2.5, and 5 μg/mL) were added and cultured with cells for 24 h. Then, we measured cell viability in the same way.

In Vivo Imaging of Early Atherosclerotic Plaques. Six-week-old apolipoprotein E-deficient (ApoE^{−/−}) mice were fed a high-fat diet for 4–6 weeks and underwent right common carotid artery narrowing. Saline, CBNP (0.3 mg/kg Ce6 and BTPO), and PM@CBNP (0.3 mg/kg Ce6 and BTPO) were injected into the tail vein twice a week for 4 weeks. Carotid artery T1 and T2 imaging was performed in mice using a small animal magnetic resonance instrument. Mice were executed, and the aorta and other major organs were collected. Fluorescence imaging of isolated tissues was performed using an IVIS-100 imaging system (Xenogen, Alameda, CA).

Biosafety. Blood was taken from healthy C57BL/6 mice into an anticoagulation tube at 1000 rpm for 10 min and centrifuged, the supernatant was discarded and washed with saline until the upper layer was essentially colorless, and the supernatant was discarded again. The blood cells were diluted to a 5% concentration with PBS and mixed 1:1 with 10, 20, and 40 mg/mL of CBNP and PM@CBNP. PBS was used as a negative control, and ddH₂O was used as a positive control. The blood cells were incubated for 4 h at 37 °C, followed by centrifugation at 3000 rpm for 10 min. The hemolytic status was recorded, and absorbance was measured at 540 nm. The hemolysis rate (HR) of the samples was calculated as follows:

$$\text{HR} = \frac{\text{OD}_{\text{sample}} - \text{OD}_{\text{saline}}}{\text{OD}_{\text{water}} - \text{OD}_{\text{saline}}} \times 100\% \quad (2)$$

For safety evaluation, major organs (heart, liver, spleen, lung, and kidney) were collected and fixed with 4% PFA. Histological analysis was performed by hematoxylin–eosin (H&E) staining.

Statistical Analysis. Results are presented as the mean ± standard deviation (SD). Statistical comparisons were made by one-way ANOVA (between two groups). The difference between the two groups was also analyzed using a two-sample *t*-test. Data analysis and figures were prepared using the GraphPad Prism software (Version 9.0) and Origin 2021. **p* < 0.05, ***p* < 0.01, ****p* < 0.001, and *****p* < 0.0001. n.s.: not significant.

■ ASSOCIATED CONTENT

Data Availability Statement

Additional data can be found in the [supplementary document](#). The data that support the findings of this study are available from the corresponding author upon reasonable request.

■ Supporting Information

The Supporting Information is available free of charge at <https://pubs.acs.org/doi/10.1021/acsami.5c10093>.

XPS of CBNP and PM@CBNP, stability over 14 days, fluorescence kinetic profiles of Ce6 and CBNP, endocytosis blocking assay, apoptosis and pyroptosis validation, and mouse biochemical index assay data ([PDF](#))

■ AUTHOR INFORMATION

Corresponding Author

Dan Mu – Department of Radiology, Nanjing Drum Tower Hospital Clinical College of Nanjing University of Chinese

Medicine, Nanjing 210008, China; Department of Radiology, Shanghai Tenth People's Hospital, Tongji University School of Medicine, Shanghai 200072, China; Yizheng Hospital of Nanjing Drum Tower Hospital Group, Living Area of Sinopec Yizheng Chemical Fibre CO.; LTD., Yizheng, Jiangsu 211900, China; Email: mudan118@126.com

Authors

Qianru Zhou – Department of Radiology, Nanjing Drum Tower Hospital Clinical College of Nanjing University of Chinese Medicine, Nanjing 210008, China; orcid.org/0009-0000-2879-789X

Maoqing Huang – Department of Radiology, Nanjing Drum Tower Hospital Clinical College of Nanjing University of Chinese Medicine, Nanjing 210008, China

Yujie Wang – Department of Radiology, Nanjing Drum Tower Hospital Clinical College of Jiangsu University, Nanjing 210008, China

Complete contact information is available at:
<https://pubs.acs.org/10.1021/acsami.5c10093>

Author Contributions

*Q.Z. and M.H. equally contributed to this work.

Notes

All animal experiments were performed in accordance with the Guidelines for the Protection and Use of Laboratory Animals of the National Institutes of Health and were approved by the Ethical Review Committee of Nanjing Drum Tower Hospital (Serial number: DWSY-24048504).

The authors declare no competing financial interest.

ACKNOWLEDGMENTS

This work was supported by the National Natural Science Foundation of China (82272065); Medical Research Project of Jiangsu Health Commission in 2022 (M2022066); the Nanjing Medical Science and technique Development Foundation (ZKX23019, ZKX19018); the 15th Special Supported Project of China Postdoctoral Science Foundation (2022 T150317), and Nanjing Gulou Hospital New Technology Development Fund (XJSFZJJ202026, XJSFZLX202114).

REFERENCES

- (1) Kong, P.; Cui, Z.; Huang, X.; Zhang, D.; Guo, R.; Han, M. Inflammation and atherosclerosis: signaling pathways and therapeutic intervention. *Signal Transduct. Target Ther.* **2022**, *7* (1), 131.
- (2) Tao, W.; Yurdagul, A.; Kong, N., Jr.; Li, W.; Wang, X.; Doran, A. C.; Feng, C.; Wang, J.; Islam, M. A.; Farokhzad, O. C.; Tabas, I.; Shi, J. siRNA nanoparticles targeting CaMKII γ in lesional macrophages improve atherosclerotic plaque stability in mice. *Sci. Transl. Med.* **2020**, *12*, No. eaay1063.
- (3) Libby, P.; Buring, J. E.; Badimon, L.; Hansson, G. K.; Deanfield, J.; Bittencourt, M. S.; Tokgozoglu, L.; Lewis, E. F. Atherosclerosis. *Nat. Rev. Dis. Primers* **2019**, *5* (1), 56.
- (4) Tian, S.; Li, Y.; Pei, H.; Tian, Y.; Zuo, Z.; Zhao, X.; Liu, C.; Zhao, Z. The pathogenesis and drug therapy of hyperlipidemia. *Chem. Life* **2022**, *42* (12), 2237–2247.
- (5) Libby, P. Inflammation during the life cycle of the atherosclerotic plaque. *Cardiovasc. Res.* **2021**, *117* (13), 2525–2536.
- (6) Doran, A. C. Inflammation Resolution: Implications for Atherosclerosis. *Circ. Res.* **2022**, *130* (1), 130–148.
- (7) Wang, W.; Zhu, H.; Gu, B.; Xie, Y.; Xu, X.; Liu, S.; Song, H. Polarity Sensitive and H₂O₂/Lipid Droplets Sequence-Activated Asymmetric Cyanine Probe Achieves Multi-marker Imaging of Atherosclerosis. *Chin. J. Chem.* **2025**, *43* (11), 1246–1254.
- (8) Li, J.; Li, Q.; Chen, C. Advances in Research on the Role of Immune Cells in the Process of Atherosclerosis. *Prog. Pharm. Sci.* **2023**, *47* (7), 542–550.
- (9) Zhang, T.; Tang, Q. Application of lipid nanoparticles in cardiovascular diseases. *Med. J. Wuhan Univ.* **2023**, 1–4.
- (10) Ma, B.; Xu, H.; Wang, Y.; Yang, L.; Zhuang, W.; Li, G.; Wang, Y. Biomimetic-Coated Nanoplatform with Lipid-Specific Imaging and ROS Responsiveness for Atherosclerosis-Targeted Theranostics. *ACS Appl. Mater. Interfaces* **2021**, *13* (30), 35410–35421.
- (11) Allen, S. D.; Liu, Y.; Kim, T.; Bobbala, S.; Yi, X.; Zhang, J.; Choi, J.; Scott, E. A. Celastrol-loaded PEG-b-PPS nanocarriers as an anti-inflammatory treatment for atherosclerosis. *Biomater. Sci.* **2019**, *7* (2), 657–668.
- (12) Xiao, X.; Chen, J.; Li, C.; Wu, M.; Li, J.; Shi, C.; Wu, S.; Li, W. Clinical application and pharmacokinetic study of nanocarriers in drug delivery system. *Acta. Pharm. Sin.* **2023**, *58* (4), 856–866.
- (13) Liu, X.; Li, Y.; Sun, Y.; Chen, B.; Du, W.; Li, Y.; Gu, N. Construction of functional magnetic scaffold with temperature control switch for long-distance vascular injury. *Biomaterials* **2022**, *290*, No. 121862.
- (14) Liu, Y.; He, M.; Yuan, Y.; Nie, C.; Wei, K.; Zhang, T.; Chen, T.; Chu, X. Neutrophil-Membrane-Coated Biomimetic Metal-Organic Framework Nanoparticles for Atherosclerosis Treatment by Targeting Gene Silencing. *ACS. Nano* **2023**, *17* (8), 7721–7732.
- (15) Chai, Y.; Shanguan, L.; Yu, H.; Sun, Y.; Huang, X.; Zhu, Y.; Wang, H. Y.; Liu, Y. Near Infrared Light-Activatable Platelet-Mimicking NIR-II NO Nano-Prodrug for Precise Atherosclerosis Theranostics. *Adv. Sci.* **2024**, *11* (3), No. e2304994.
- (16) Xu, H.; She, P.; Zhao, Z.; Ma, B.; Li, G.; Wang, Y. Duplex Responsive Nanoplatform with Cascade Targeting for Atherosclerosis Photoacoustic Diagnosis and Multichannel Combination Therapy. *Adv. Mater.* **2023**, *35* (21), No. e2300439.
- (17) Liu, S.; Pan, X.; Liu, H. Two-Dimensional Nanomaterials for Photothermal Therapy. *Angew. Chem., Int. Ed. Engl.* **2020**, *59* (15), 5890–5900.
- (18) Modi, S. K.; Mohapatra, P.; Bhatt, P.; Singh, A.; Parmar, A. S.; Roy, A.; Joshi, V.; Singh, M. S. Targeting tumor microenvironment with photodynamic nanomedicine. *Med. Res. Rev.* **2025**, *45* (1), 66–96.
- (19) Mu, D.; Wang, X.; Wang, H.; Sun, X.; Dai, Q.; Lv, P.; Liu, R.; Qi, Y.; Xie, J.; Xu, B.; Zhang, B. Chemiexcited Photodynamic Therapy Integrated in Polymeric Nanoparticles Capable of MRI Against Atherosclerosis. *Int. J. Nanomed.* **2022**, *17*, 2353–2366.
- (20) Liu, J.; Zhou, B.; Guo, Y.; Zhang, A.; Yang, K.; He, Y.; Wang, J.; Cheng, Y.; Cui, D. SR-A-Targeted Nanoplatform for Sequential Photothermal/Photodynamic Ablation of Activated Macrophages to Alleviate Atherosclerosis. *ACS Appl. Mater. Interfaces* **2021**, *13* (25), 29349–29362.
- (21) Hu, Y.; Gao, X.; Ma, J.; Shanguan, Z.; Chen, L.; Zhang, G.; Zhang, X.; Li, C.; Li, Y.; Zhang, D. New AIE Emitters from the Unexpected Boron Tribromide/Boron Trichloride-mediated Cyclization Reaction and Application for Fluorescence Imaging of Lipid Droplets. *Aggregate* **2025**, *6* (4), No. e735.
- (22) Zhang, F.; Zhang, Y.; Li, Z.; Wu, X.; Wang, D.; He, Y.; Cheng, H.; Fan, B.; Zhu, D.; Li, M.; Tang, B. Z. Engineered Strategies for Lipid Droplets-Targeted AIEgens Based on Tetraphenylethene. *Molecules* **2024**, *29* (24), 5904.
- (23) Lei, X.; Zheng, J.; Chen, X.; Liang, L.; Li, Z.; Huang, C.; Zhao, M.; Wu, G.; Liao, Y.; Yang, B. Highly Stable Aggregation-Induced Emission-Functionalized Histatin1 Coated With Platelet Vesicles for Diabetic Wound Healing. *Aggregate* **2025**, *6* (7), No. e7003.
- (24) Ding, J.; Lu, G.; Nie, W.; Huang, L. L.; Zhang, Y.; Fan, W.; Wu, G.; Liu, H.; Xie, H. Y. Self-Activatable Photo-Extracellular Vesicle for Synergistic Trimodal Anticancer Therapy. *Adv. Mater.* **2021**, *33* (7), No. e2005562.
- (25) Ran, Z.; Wang, M.; Yuan, Z.; Zhang, Y.; Liu, G.; Yang, R. Acid-responsive singlet oxygen nanodepots. *Chem. Sci.* **2025**, *16* (3), 1197–1204.

- (26) Wu, H.; Wang, L.; Wang, Y.; Shao, Y.; Li, G.; Shao, K.; Akkaya, E. U. Targeted Singlet Oxygen Delivery: A Bioorthogonal Metabolic Shunt Linking Hypoxia to Fast Singlet Oxygen Release. *Angew. Chem., Int. Ed. Engl.* **2022**, 61 (47), No. e202210249.
- (27) Turan, I. S.; Yildiz, D.; Turksoy, A.; Gunaydin, G.; Akkaya, E. U. A Bifunctional Photosensitizer for Enhanced Fractional Photodynamic Therapy: Singlet Oxygen Generation in the Presence and Absence of Light. *Angew. Chem., Int. Ed. Engl.* **2016**, 55 (8), 2875–2878.
- (28) Zou, J.; Yin, Z.; Wang, P.; Chen, D.; Shao, J.; Zhang, Q.; Sun, L.; Huang, W.; Dong, X. Photosensitizer synergistic effects: D-A-D structured organic molecule with enhanced fluorescence and singlet oxygen quantum yield for photodynamic therapy. *Chem. Sci.* **2018**, 9 (8), 2188–2194.
- (29) Chen, L.; Zhou, Z.; Hu, C.; Maitz, M. F.; Yang, L.; Luo, R.; Wang, Y. Platelet Membrane-Coated Nanocarriers Targeting Plaques to Deliver Anti-CD47 Antibody for Atherosclerotic Therapy. *Research* **2022**, No. 9845459.
- (30) Song, Y.; Huang, Z.; Liu, X.; Pang, Z.; Chen, J.; Yang, H.; Zhang, N.; Cao, Z.; Liu, M.; Cao, J.; Li, C.; Yang, X.; Gong, H.; Qian, J.; Ge, J. Platelet membrane-coated nanoparticle-mediated targeting delivery of Rapamycin blocks atherosclerotic plaque development and stabilizes plaque in apolipoprotein E-deficient (ApoE^{-/-}) mice. *Nanomed. Nanotechnol. Biol. Med.* **2019**, 15 (1), 13–24.
- (31) Xie, L.; Chen, J.; Hu, H.; Zhu, Y.; Wang, X.; Zhou, S.; Wang, F.; Xiang, M. Engineered M2 macrophage-derived extracellular vesicles with platelet membrane fusion for targeted therapy of atherosclerosis. *Bioact Mater.* **2024**, 35, 447–460.
- (32) Hu, S.; Wang, X.; Li, Z.; Zhu, D.; Cores, J.; Wang, Z.; Li, J.; Mei, X.; Cheng, X.; Su, T.; Cheng, K. Platelet membrane and stem cell exosome hybrid enhances cellular uptake and targeting to heart injury. *Nano Today* **2021**, 39, No. 101210.
- (33) Kappelmayer, J.; Nagy, B., Jr. The Interaction of Selectins and PSGL-1 as a Key Component in Thrombus Formation and Cancer Progression. *BioMed. Res. Int.* **2017**, No. 6138145.
- (34) Shen, C.; Mackeigan, D. T.; Shoara, A. A.; Xu, R.; Bhorla, P.; Karakas, D.; Ma, W.; Cerenzia, E.; Chen, Z.; Hoard, B.; Lin, L.; Lei, X.; Zhu, G.; Chen, P.; Johnson, P. E.; Ni, H. Dual roles of fucoidan-GPIIb α interaction in thrombosis and hemostasis: implications for drug development targeting GPIIb α . *J. Thromb Haemost* **2023**, 21 (5), 1274–1288.
- (35) Li, J.; Li, Q.; Chen, C. Advances in Research on the Role of Immune Cells in the Process of Atherosclerosis. *Progr. Pharm. Sci.* **2023**, 47 (7), 542–550.
- (36) Chen, Y.; Zhang, J.; Cui, W.; Silverstein, R. L. CD36, a signaling receptor and fatty acid transporter that regulates immune cell metabolism and fate. *J. Exp. Med.* **2022**, 219 (6), No. e20211314.
- (37) Karunakaran, D.; Nguyen, M. A.; Geoffrion, M.; Vreeken, D.; Lister, Z.; Cheng, H.; Otte, N.; Essebier, P.; Wyatt, H.; Kandiah, J. W.; Jung, R.; Alenghat, F. J.; Mompeon, A.; R; Lee, C.; Pan, Gordon E.; Rasheed, A.; Lusis, A. J.; Liu, P.; Matic, L. P.; Hedin, U.; Fish, J. E.; Guo, L.; Kolodgie, F.; Virmani, R.; van Gils, J. M.; Rayner, K. J. RIPK1 Expression Associates With Inflammation in Early Atherosclerosis in Humans and Can Be Therapeutically Silenced to Reduce NF- κ B Activation and Atherogenesis in Mice. *Circulation* **2021**, 143 (2), 163–177.
- (38) Shu, H.; Peng, Y.; Hang, W.; Nie, J.; Zhou, N.; Wang, D. W. The role of CD36 in cardiovascular disease. *Cardiovasc. Res.* **2022**, 118 (1), 115–129.
- (39) Mou, X.; Wu, Q.; Zhang, Z.; Liu, Y.; Zhang, J.; Zhang, C.; Chen, X.; Fan, K.; Liu, H. Nanozymes for Regenerative Medicine. *Small Methods* **2022**, 6 (11), No. e2200997.
- (40) Zhang, Y.; Liu, W.; Wang, X.; Liu, Y.; Wei, H. Nanozyme-Enabled Treatment of Cardio-and Cerebrovascular Diseases. *Small* **2022**, 9 (13), No. e2204809.
- (41) Wang, S.; Zhang, J.; Li, W.; Chen, D.; Tu, J.; Sun, C.; Du, Y. Hyaluronic Acid-Guided Assembly of Ceria Nanozymes as Plaque-Targeting ROS Scavengers for Anti-Atherosclerotic Therapy. *Carbohydr. Polym.* **2022**, 296, No. 119940.
- (42) Fu, X.; Yu, X.; Jiang, J.; Yang, J.; Chen, L.; Yang, Z.; Yu, C. Small Molecule-Assisted Assembly of Multifunctional Ceria Nanozymes for Synergistic Treatment of Atherosclerosis. *Nat. Commun.* **2022**, 13, 6528.
- (43) Wang, S.; Zhou, Y.; Liang, X.; Xu, M.; Li, N.; Zhao, K. Platinum-Cerium Bimetallic Nano-Raspberry for Atherosclerosis Treatment via Synergistic Foam Cell Inhibition and P2Y12 Targeted Antiplatelet Aggregation. *Chem. Eng. J.* **2022**, 430, No. 132859.
- (44) Li, Y.; Wu, J.; Qiu, X.; Dong, S.; He, J.; Liu, J.; Xu, W.; Huang, S.; Hu, X.; Xiang, D. X. Bacterial outer membrane vesicles-based therapeutic platform eradicates triple-negative breast tumor by combinational photodynamic/chemo-/immunotherapy. *Bioact Mater.* **2023**, 20, 548–560.
- (45) Hu, Y.; Zhang, C.; Li, S.; Jiao, Y.; Qi, T.; Wei, G.; Han, G. Effects of Photodynamic Therapy Using Yellow LED-light with Concomitant Hypocrellin B on Apoptotic Signaling in Keloid Fibroblasts. *Int. J. Biol. Sci.* **2017**, 13 (3), 319–326.
- (46) Goloroush, P.; Yellon, D. M.; Davidson, S. M. Mouse models of atherosclerosis and their suitability for the study of myocardial infarction. *Basic Res. Cardiol.* **2020**, 115 (6), 73.
- (47) Ma, Y.; Wang, W.; Zhang, J.; Lu, Y.; Wu, W. Hyperlipidemia and atherosclerotic lesion development in Ldlr-deficient mice on a long-term high-fat diet. *PLoS One* **2012**, 7 (4), No. e35835.



CAS BIOFINDER DISCOVERY PLATFORM™

CAS BIOFINDER HELPS YOU FIND YOUR NEXT BREAKTHROUGH FASTER

Navigate pathways, targets, and
diseases with precision

Explore CAS BioFinder



A division of the
American Chemical Society